nature nanotechnology

LETTERS

https://doi.org/10.1038/s41565-020-0700-y

Check for updates

Flexoelectronics of centrosymmetric semiconductors

Longfei Wang[1,2,3,8], Shuhai Liu[4,8], Xiaolong Feng[5,8], Chunli Zhang[6,8], Laipan Zhu[1,2], Junyi Zhai[1,2], Yong Qin[7] ✉ and Zhong Lin Wang[1,3] ✉

Interface engineering by local polarization using piezoelectric[1–4], pyroelectric[5,6] and ferroelectric[7–9] effects has attracted considerable attention as a promising approach for tunable electronics/optoelectronics, human–machine interfacing and artificial intelligence. However, this approach has mainly been applied to non-centrosymmetric semiconductors, such as wurtzite-structured ZnO and GaN, limiting its practical applications. Here we demonstrate an electronic regulation mechanism, the flexoelectronics, which is applicable to any semiconductor type, expanding flexoelectricity[10–13] to conventional semiconductors such as Si, Ge and GaAs. The inner-crystal polarization potential generated by the flexoelectric field serving as a 'gate' can be used to modulate the metal–semiconductor interface Schottky barrier and further tune charge-carrier transport. We observe a giant flexoelectronic effect in bulk centrosymmetric semiconductors of Si, TiO_2 and Nb-$SrTiO_3$ with high strain sensitivity (>2,650), largely outperforming state-of-the-art Si-nanowire strain sensors and even piezoresistive, piezoelectric and ferroelectric nanodevices[14]. The effect can be used to mechanically switch the electronics in the nanoscale with fast response (<4 ms) and high resolution (~0.78 nm). This opens up the possibility of realizing strain-modulated electronics in centrosymmetric semiconductors, paving the way for local polarization field-controlled electronics and high-performance electromechanical applications.

The concept of flexoelectronics is schematically shown in Fig. 1a. When an inhomogeneous strain or stress is induced in a semiconductor, a flexoelectric polarization field can be generated due to the flexoelectric effect[15–18] (Supplementary Note 1); this field not only presents on the material surface but also distributes inside the crystal over a range of lengths or volumes owing to the enormous non-uniform local strain. The inner-crystal polarization field has a huge impact on the concentration and distribution of free carriers at the metal–semiconductor interface as well as inside the semiconductor (Fig. 1a(i)), resulting in band-structure engineering of both the metal–semiconductor interface and the inner crystal. In general, the negative flexoelectric polarization potential induced at the semiconductor side can repel electrons while attracting holes near the interface, enabling the energy band to be bent upward. Thus, strain-gradient-induced flexoelectric polarization can effectively modulate the interface Schottky barrier height and width, thereby controlling the charge transport (Fig. 1a(ii)), in a manner analogous to the piezotronic effect[19–22]. The magnitude and polarity of the flexoelectric potential depend on that of the applied inhomogeneous stress or strain, respectively. This is the flexoelectronic effect, which is universal and persistent and exists widely in most semiconductors. The use of the inner-crystal flexoelectric polarization potential as a 'gate' controlling signal to modulate the barrier profile and achieve a tunable electronic process is the basis of flexoelectronics (Fig. 1a(iii)).

We explored the flexoelectronic effect induced by a point force applied to the surface of a Si single crystal. The point force, applied by an atomic force microscope tip, induced local inhomogeneous strain at the tip–surface contact, which caused a localized breaking of centrosymmetry. The direct-current electrical transport properties of the devices under nanoindentations were simultaneously characterized using a conductive atomic force microscopy (AFM) measurement system. The atomic force microscope tip can be approximated as a hemisphere, and hence the spatial distribution of the strain gradient can be calculated analytically from Hertzian contact theory[23] (Methods and Supplementary Note 2). The calculated strain distribution in Si in terms of both the x and z components, and the derivative of this strain distribution with respect to z, are shown in Fig. 1b and Supplementary Fig. 1, respectively. The calculated strain gradient is as high as $10^6\,m^{-1}$, which is much higher than those achievable using conventional micrometre-/nanometre-thick beam-bending approaches (which achieve gradients in the range of $\sim10^{-1}$–$10^2\,m^{-1}$) (refs. [15,24]). In fact, the strain gradient in the experiment may be smaller than the theoretical results because in the calculations the tip is assumed to have infinite rigidity. Figure 1c shows the simulated flexoelectric polarization distribution corresponding to the same mechanical loading conditions. The out-of-plane polarization P reaches a maximum of $\sim0.03\,C\,m^{-2}$ beneath the centre of the contact region. In fact, experimental values are orders of magnitude higher than the simulated results. The main reason for this discrepancy is that the theoretical effective flexoelectric coefficients (u_{eff}) are calculated at 0 K and the materials are generally considered as intrinsic crystals without defects, whereas the experimental results are usually obtained at room temperature and depend strongly on both the amount of doping and the static dielectric constant of the sample[25]. For example, experimental flexoelectric coefficients of

[1]Beijing Institute of Nanoenergy and Nanosystems, Chinese Academy of Sciences, Beijing, P. R. China. [2]School of Nanoscience and Technology, University of Chinese Academy of Sciences, Beijing, P. R. China. [3]School of Material Science and Engineering, Georgia Institute of Technology, Atlanta, GA, USA. [4]School of Advanced Materials and Nanotechnology, Xidian University, Xi'an, P. R. China. [5]Research Laboratory for Quantum Materials, Singapore University of Technology and Design, Singapore, Singapore. [6]Key Laboratory of Soft Machines and Smart Devices of Zhejiang Province, Department of Engineering Mechanics, Zhejiang University, Hangzhou, P. R. China. [7]Institute of Nanoscience and Nanotechnology, School of Physical Science and Technology, Lanzhou University, Gansu, P. R. China. [8]These authors contributed equally: Longfei Wang, Shuhai Liu, Xiaolong Feng, Chunli Zhang. ✉e-mail: qinyong@lzu.edu.cn; zhong.wang@mse.gatech.edu

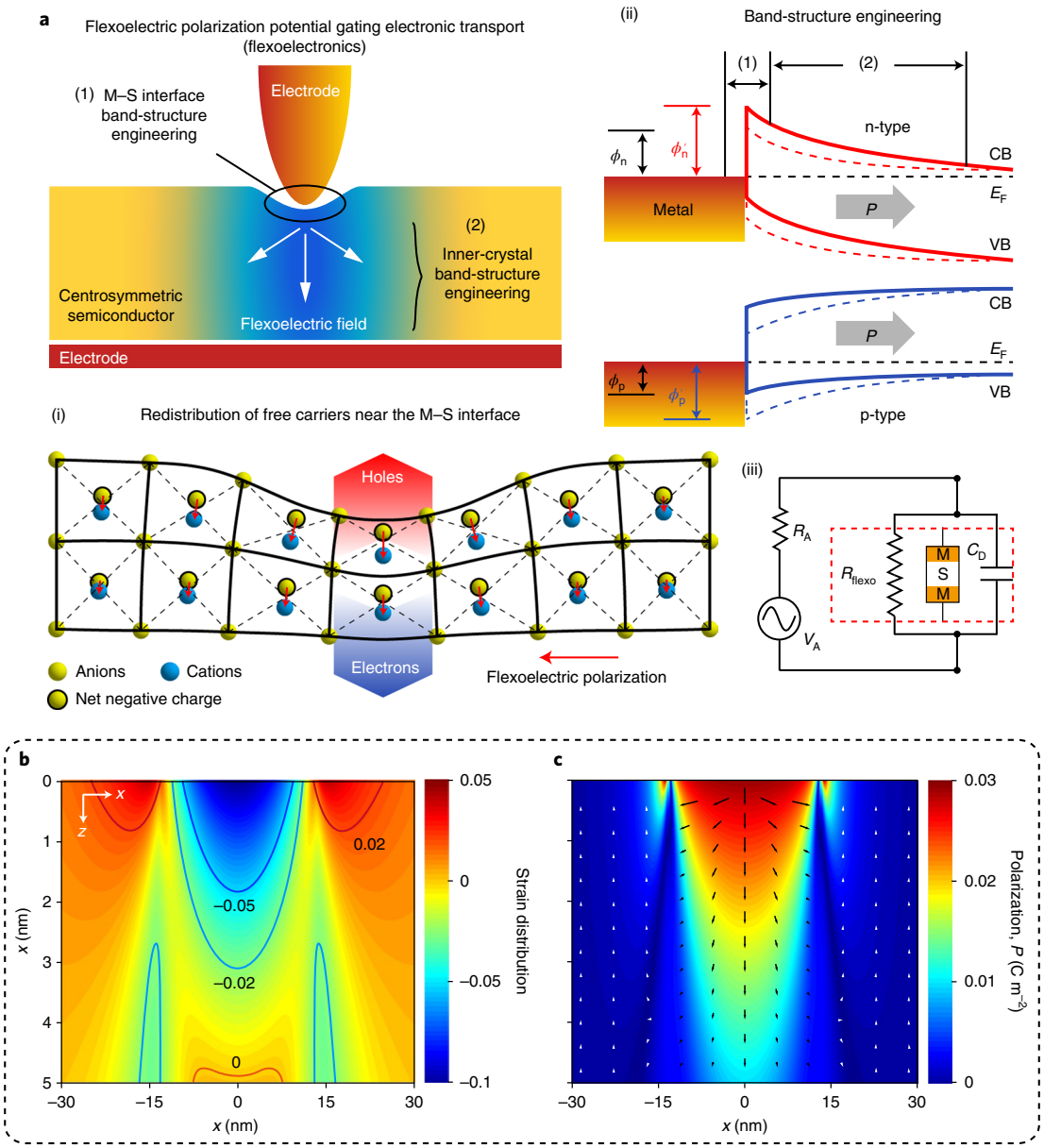

Fig. 1 | The mechanism of flexoelectronics. a, Schematic showing the concept of flexoelectronics proposed here, according to which the flexoelectric polarization potential generated in a centrosymmetric semiconductor gates the electronic transport. (i) Inhomogeneous strained centrosymmetric crystal structure. A flexoelectric built-in electric field formed in a centrosymmetric semiconductor exerts a substantial influence on the concentration and distribution of free carriers near the interface, resulting in band-structure engineering ((ii)) that involves (1) metal–semiconductor (M–S) interface band-structure engineering and (2) inner-crystal band-structure engineering, and is a result of the changes in Schottky barrier height. This is the flexoelectronic effect. ϕ_n/ϕ'_n and ϕ_p/ϕ'_p represent the Schottky barrier heights formed between metal and n-type and p-type semiconductor contacts without (dashed line) and with (solid line) strain, respectively. CB, VB and E_F represent the conduction band, valence band and Fermi surface, respectively. The red and blue lines represent the band structures of the n-type semiconductor and p-type semiconductor, respectively. The grey arrows represent the magnitude and direction of flexoelectric polarization under nanoindentation. (iii), Equivalent circuit diagram for the flexoelectronics. The region delineated by red dashed lines is a two-terminal device, in which R_{flexo} represents the equivalent tunable resistor modulated by a strain gradient. Using the strain-gradient-induced inner-crystal flexoelectric polarization potential as a 'gate' controlling signal to modulate the interface barrier profile and achieve tunable electronic process is the flexoelectronics. R_A, V_A and C_D represent the series resistor, voltage source and equivalent parallel capacitance, respectively. **b**,**c**, Flexoelectricity in Si obtained from theoretical simulations with a tip-force model, showing the corresponding strain distribution (**b**) and the flexoelectric polarization distribution (**c**) under a tip force of 25 μN. Arrows in **c** denote the polarization direction. The force is directed downward by the atomic force microscope tip (radius, 25 nm), which is centred at the origin.

Si as high as ~78 nC m^{-1} have been reported, whereas the theoretical values are only ~1 nC m^{-1} (ref. [25]). Additionally, a nonlinear flexoelectric response occurs under large strain gradients, which may enhance the flexocoupling coefficient (Supplementary Note 3).

We characterized the electrical transport properties of a commercial p-type Si single crystal with low doping under atomic force microscope tip indentations. For the device, the current–voltage (I–V) characteristics exhibit typical rectification behaviour and

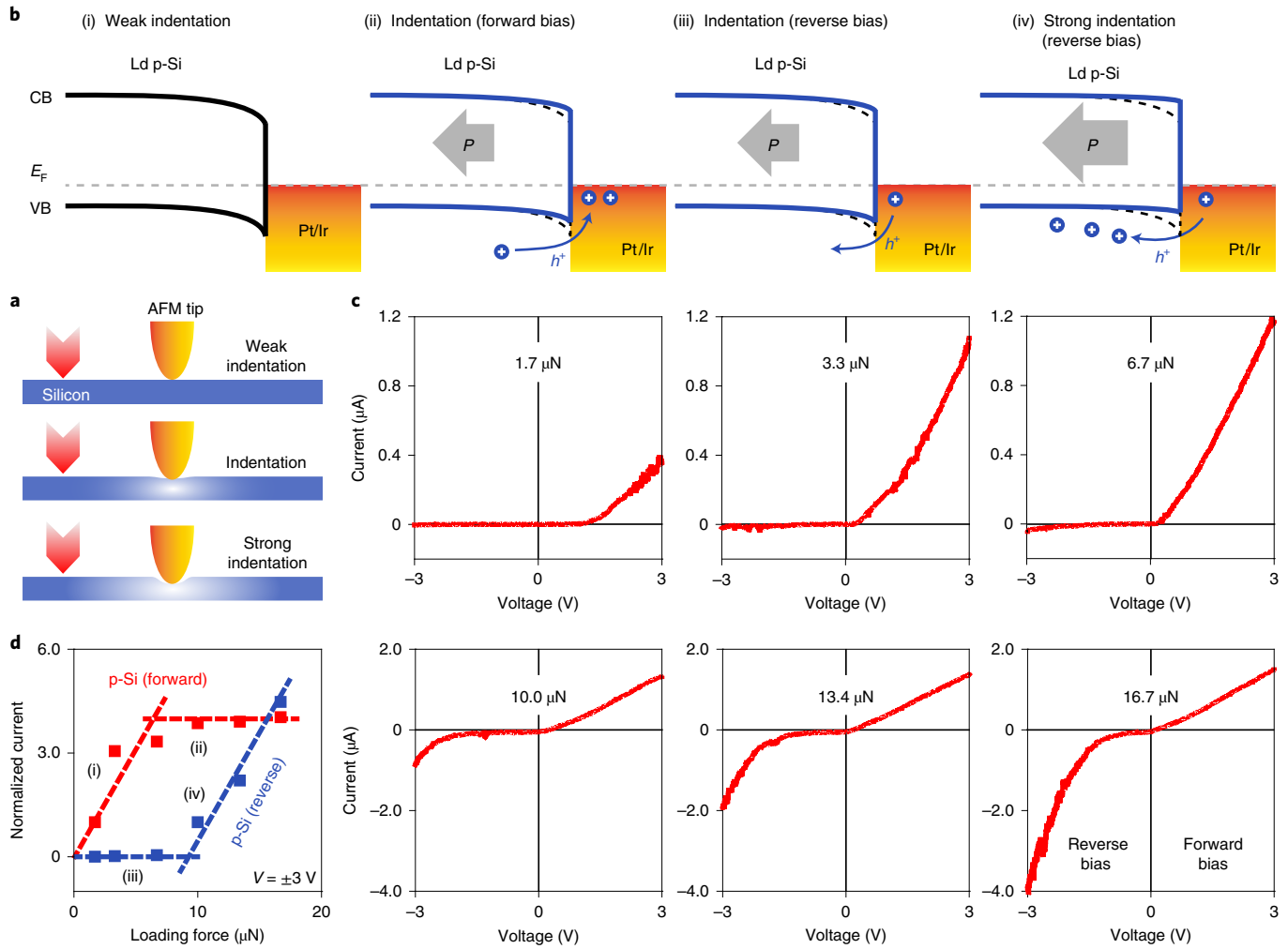

Fig. 2 | Flexoelectronic effect in low-doped p-Si single crystal. a, Schematic of the experimental setup illustrating the change in contact between an atomic force microscope tip and sample as the contact force increases. The red arrowheads represent the process of contact. **b**, Band diagrams showing the mechanism of the modulation process in low-doped (Ld) p-Si single crystal (~10 Ω cm), corresponding to the change in contact shown in **a**. The blue solid lines and the black dashed lines represent the energy-band profiles with and without flexoelectric polarization, respectively. The grey arrows represent the magnitude and direction of flexoelectric polarization under nanoindentation. **c**, The asymmetric modulation of electrical transport by a flexoelectric polarization field induced by a gradient in stress and/or strain under opposite bias in p-Si single-crystal-based devices shows the characteristics of the flexoelectronic effect. **d**, Normalized current distribution versus loading force shows the flexoelectronic process in low-doped p-Si, corresponding to the changes in the band diagrams shown in **b**. Labels (i) to (iv) represent the stages of current change under loading forces.

are highly asymmetric (Fig. 2c and Supplementary Fig. 3). The forward current increases steadily with the increase in loading force, whereas the reverse current remains comparable to the noise level, which corresponds to the processes shown in Fig. 2d(i) and (ii), respectively. The *I*–*V* characteristic becomes maximally asymmetric at a critical force of ~7 μN. As the force continues to increase, however, the reverse current begins to increase substantially, whereas the forward current is only slightly increased, corresponding to the processes in Fig. 2d(ii),(iv). A gauge factor of bulk p-Si of >2,650 is measured in our experiments (Methods), which is orders of magnitude larger than that of conventional bulk strain sensors (~0.7–11.45) and a state-of-the-art Si-nanowire strain sensor (~200), and even considerably higher than the values of piezoresistive/piezoelectric/ferroelectric nanosensors (~2–2,000)[14,26] (Supplementary Table 1).

This anomalous behaviour cannot be explained simply by the increase in contact area and the piezoresistive effect[27]. First, the local deformation on the p-Si surface caused by tip-induced non-uniform strain will increase the tip–surface contact area and create a piezoresistive effect (Supplementary Fig. 4). However, the piezoresistive effect is a symmetric volume effect without polarity, in which a change in the strain-induced bandgap or charge-carrier density can modulate the entire resistance of Si, and hence the *I*–*V* curve should change symmetrically from forward bias to reverse bias. Our theoretical analysis also shows that the piezoresistive effect in bulk Si is too small to be responsible for our observations (Supplementary Fig. 5). Second, mechanical control of electrical transport in the p-Si is highly asymmetric and reversible, properties that cannot be attributable only to the change in the contact area between the microscope tip and the Si surface.

The origin of this mechanically tunable electronic process is the flexoelectronic effect. Figure 2b shows the proposed mechanism of the modulation process in p-Si, corresponding to changes in contact as the loading force increases (Fig. 2a). Under weak indentation, a contact barrier exists at the metal–semiconductor interface and gradually decreases as the loading force increases (Fig. 2b(i)). Meanwhile, local strain-gradient-induced flexoelectric polarization attracts holes near the interface, resulting in a decreased interface

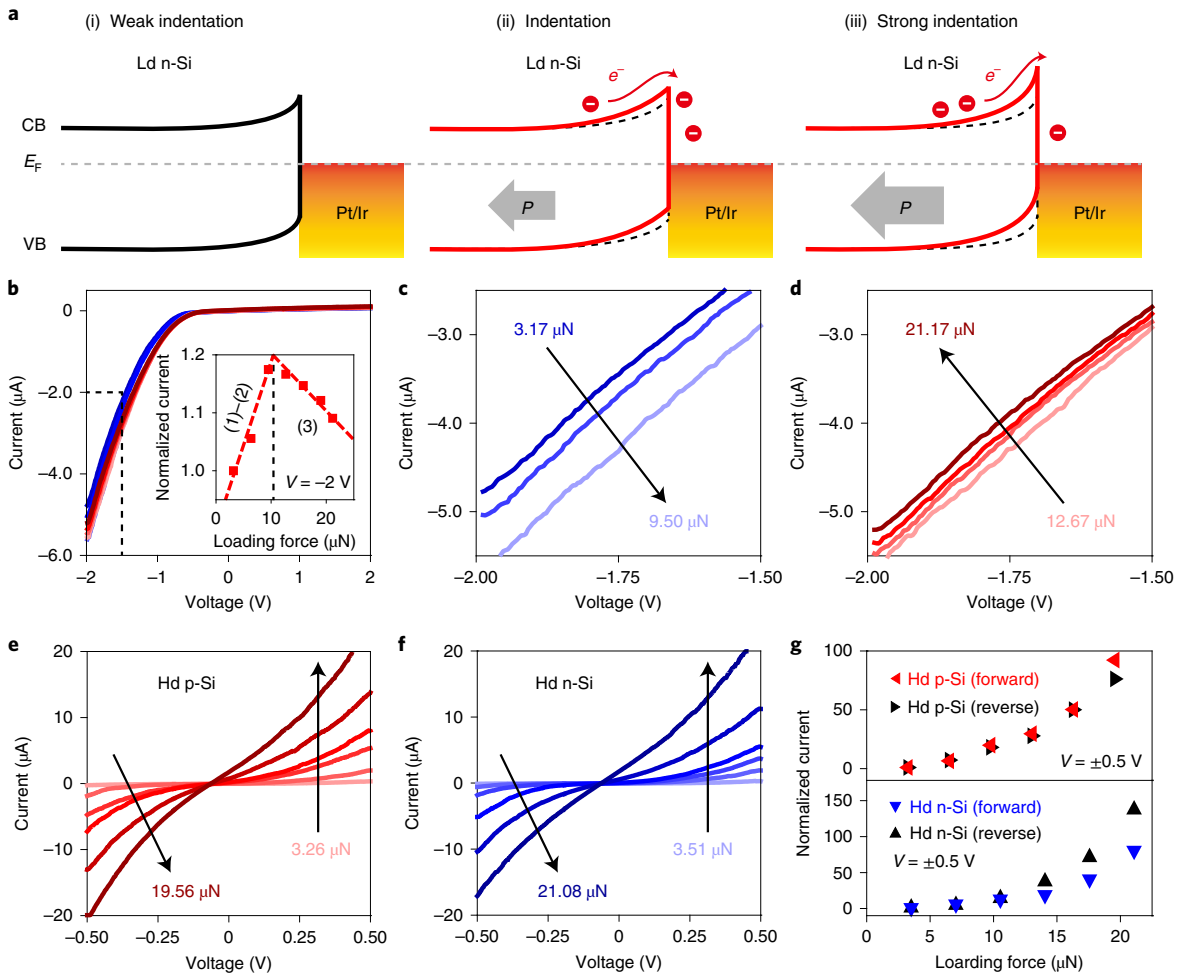

Fig. 3 | Electronic transport in other types of silicon under nanoindentation. a, Band diagrams showing the mechanism of the modulation process in low-doped (Ld) n-Si (~10 Ω cm), corresponding to the change in contact shown in Fig. 2a. The red solid lines and the black dashed lines represent the energy-band profiles with and without flexoelectric polarization, respectively. The grey arrows represent the magnitude and direction of flexoelectric polarization under nanoindentation. **b**–**d**, The reverse modulation of electronic transport by a stress-induced flexoelectric polarization field in n-Si single-crystal-based devices shows the characteristics of the flexoelectronic effect. Inset: normalized current distribution versus contact force (at a voltage of −2 V) showing the flexoelectronic process in low-doped n-Si, corresponding to the changes in the band diagrams shown in **a**. The numbers (1)–(3) in **b** refer to the stages of current change under loading forces. Panel **b** inset: The black dashed line indicates the critical force. **c** and **d** are enlarged views of the dashed frame shown in **b**. The gradient colours indicate the current change under loading forces. **e**,**f**, The symmetric modulation of carrier transport by loading forces under opposite voltage bias in heavily doped (Hd) (~0.001 Ω cm) p-type (**e**) and n-type (**f**) Si-based devices show piezoresistive-like responses. **g**, Normalized current change in devices based on heavily doped Si as a function of loading force, also showing symmetric characteristics.

barrier (Fig. 2b(ii)). The joint modulation of the two synergistic effects increases the charge transport under forward bias (Fig. 2d(i)). However, in reverse-bias mode the local barrier (Fig. 2b(iii)) is still large enough to limit the charge transport (Fig. 2d(iii)). Under strong indentation, the Schottky barrier height is greatly decreased by the strong flexoelectric polarization induced by a larger strain gradient (Fig. 2b(iv)), which improves electrical transport under the reverse bias (Fig. 2d(iv)), but has only a weak effect on electrical transport under the forward bias (Fig. 2d(ii)).

To understand in depth the flexoelectronic effect in Si, we investigated the electrical transport characteristics in low-doped n-type Si single crystal under a tip force. The current first increases steadily and then gradually decreases, reaching a maximum value at a critical force of ~10 μN, which corresponds to processes (1)–(2) and (3) shown in Fig. 3b and Supplementary Fig. 6. The reverse stages of the electrical transport modulation process can be attributed to the competition between the decrease in the contact barrier caused by the increased contact area and the strain-gradient-induced flexoelectric polarization ((i) and (ii) in Fig. 3a). As in the case of p-Si, a decrease in the contact barrier at the tip–surface interface enhances the electrical transport (Fig. 3b(1) and (2),c). Under strong indentation, the modulation effect of larger strain-gradient-induced flexoelectric polarization on the band structure begins to dominate the charge transport across the Schottky contacts ((iii) in Fig. 3a), resulting in weakened electrical transport (Fig. 3b,d). The detailed evolution of barrier height and the width of tip–Si Schottky contact under nanoindentation is shown in Supplementary Figs. 7 and 8. Theoretical simulations further reveal that flexoelectric polarization can effectively modulate the carrier distribution, interface barrier and hence the electrical transport of low-doped Si (Supplementary Figs. 9 and 10). Additionally, we also exclude the possible effect of surface contribution on the results, which is always combined with the bulk flexoelectric polarization in the case of materials under bending (Supplementary Note 4).

In reality, the presence of free charges in the Si volume may create a screening effect[28] on the flexoelectric polarization and hence

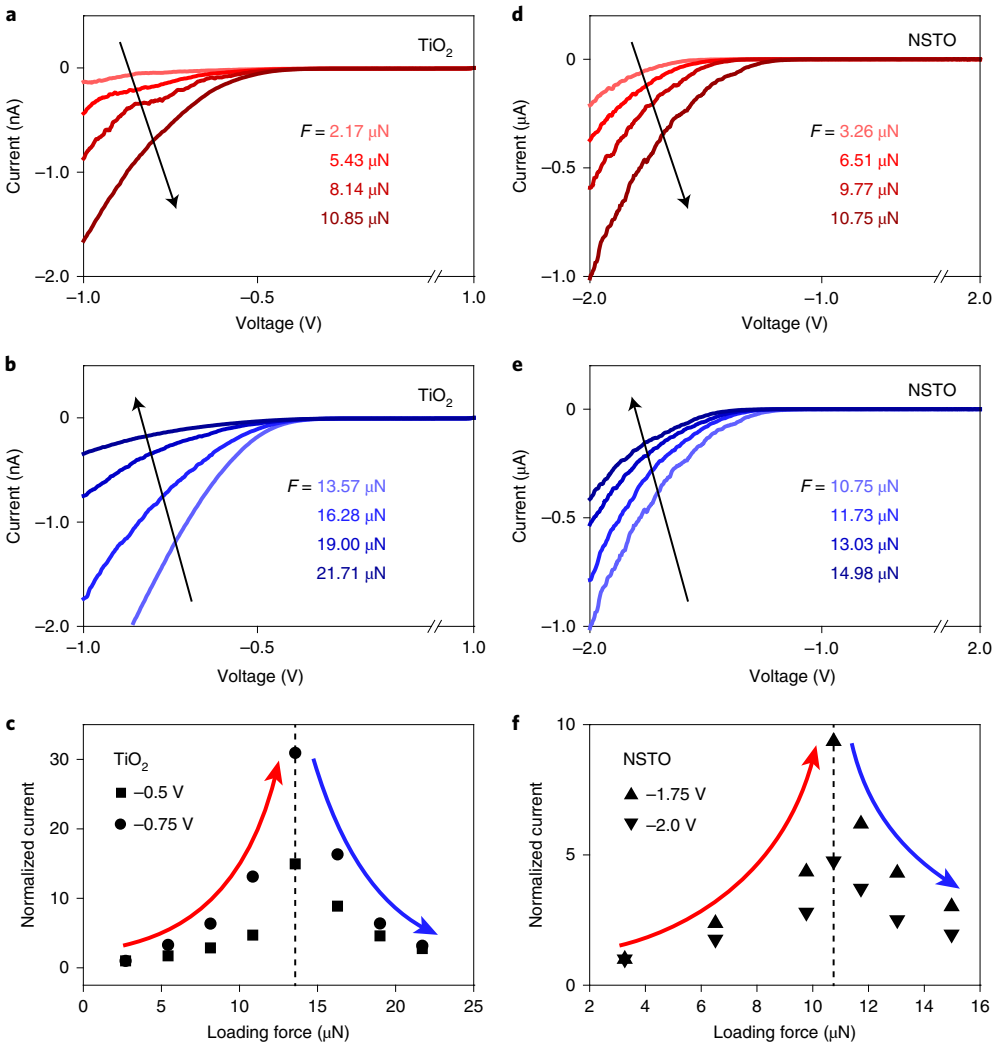

Fig. 4 | Flexoelectronic effect in ionic semiconductors. a,**b**,**d**,**e**, Current–voltage characteristics measured in single-crystal TiO_2 (**a**,**b**) and NSTO (**d**,**e**) by conductive AFM. The tip loading force is accurately controlled by the feedback loop of the atomic force microscope. The black arrows indicate the current change under loading forces. There are two distinct stages of the modulation process in electrical transport in ionic-semiconductor-based devices as the loading force increases, which indicates that two kinds of regulatory mechanism exist for electrical transport and that these resemble the modulation mechanism in low-doped n-Si-based devices. **c**,**f**, Normalized current distribution versus loading force shows the modulation process (red and blue curves) in the ionic semiconductors TiO_2 (**c**) and NSTO (**f**). The reverse modulation of electrical transport in an ionic semiconductor demonstrates the flexoelectric effect due to the flexoelectric polarization field induced by a gradient in stress and/or strain. The red and blue arrows show the two opposing modulation processes under loading forces.

reduce the flexoelectric performance (Supplementary Note 5), we nevertheless observed a flexoelectronic effect in low-doped Si due to the screening of flexoelectric polarization being only partial. However, the screening effect of free charges may be substantial in heavily doped Si. The proposed mechanism shown in Figs. 2b and 3a may therefore be invalid. We performed the same experiments on heavily doped Si crystals. In this case, the responses of the bulk Si devices are all piezoresistive in nature: the current increases symmetrically with loading force, and this effect is independent of doping type (Fig. 3e–g and Supplementary Fig. 11).

To show that the flexoelectronic effect is not limited to covalent crystals, we performed the same series of experiments with single-crystal rutile-TiO_2 and Nb–$SrTiO_3$ (NSTO). Supplementary Fig. 2 demonstrates that tip nanoindentation can produce a large strain gradient and effective flexoelectric polarization in TiO_2 and NSTO. The I–V characteristics of the TiO_2 and NSTO under mechanical loading forces are similar to those of low-doped n-Si (Fig. 4a,b,d,e and Supplementary Figs. 12 and 13). The electrical transport characteristics under loading forces are the consequence of two opposing modulation processes (Fig. 4c,f), which are mainly attributable to competition between the lowering of the contact barrier due to the increased contact area and the increase in the Schottky barrier caused by strain-gradient-induced flexoelectric polarization (Fig. 3a). To quantitatively analyse the performance of ionic semiconductor-based flexoelectronic devices further, we characterized the strain sensitivity in terms of the gauge factor. The strain sensitivity values for TiO_2 and NSTO are ~472 and ~183, respectively, which are orders of magnitude larger than those of conventional bulk strain sensors (~0.7–11.45) (refs. [14,26]) (Supplementary Table 1). The difference between TiO_2 and NSTO may be due to the more effective flexoelectric polarization of the former, which possibly results from the reduced screening effect caused by the decreased carrier concentration and mobility. The theoretical simulations also highlight the crucial role of flexoelectric polarization in the modulation process of ionic semiconductors (Supplementary Fig. 14). These results demonstrate the effectiveness and universality

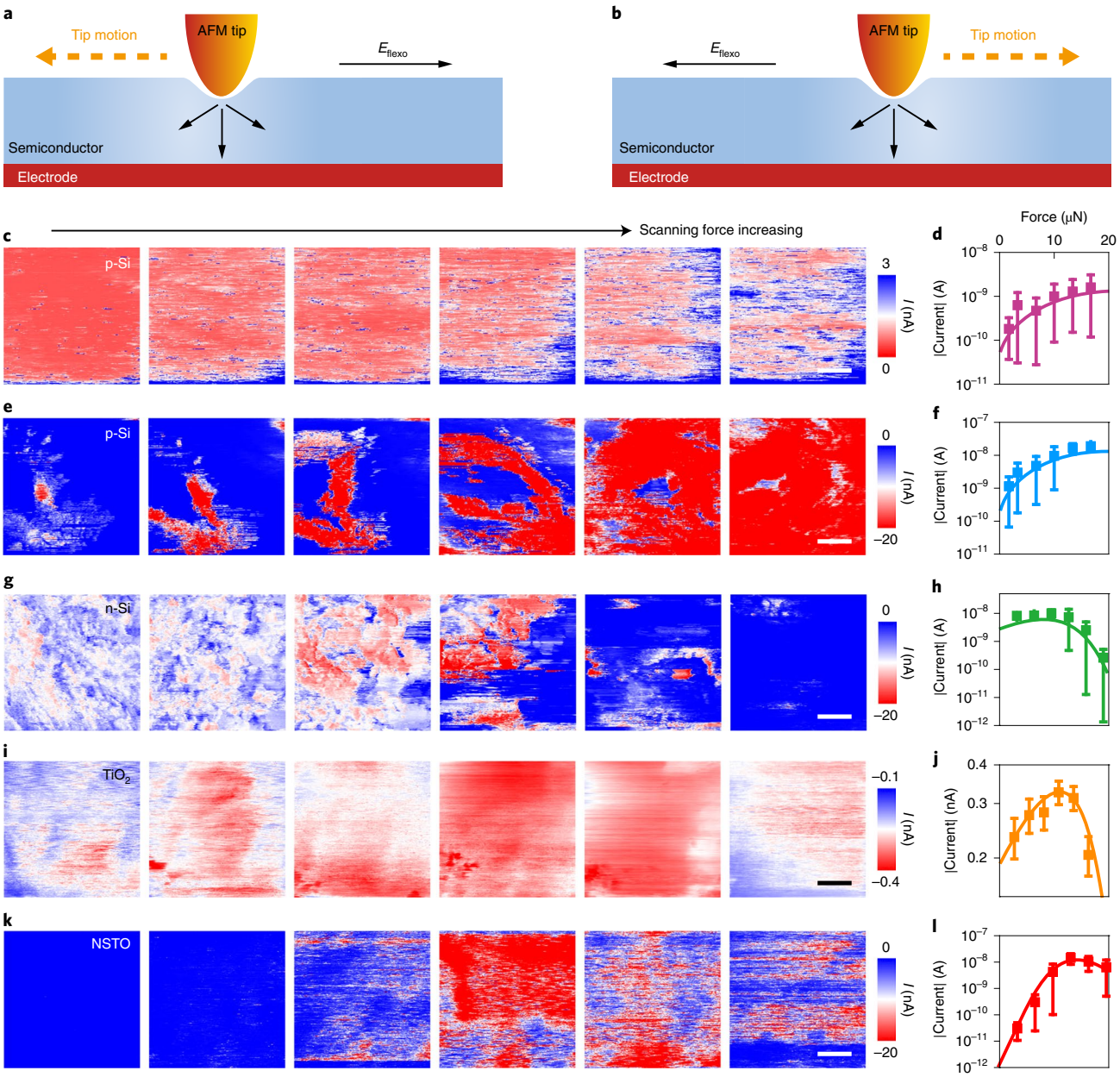

Fig. 5 | Demonstration of flexoelectronics by mechanical 2D scanning. a,**b**, Schematics illustrating mechanical 2D scanning using a probe under fixed bias and fixed contact force, and the flexoelectric polarization field (E_{flexo}) generated by the tip motion along the surface of a semiconductor. **c**,**e**,**g**,**i**,**k**, The corresponding current mappings in p-Si under a fixed forward bias of 0.5 V (**c**), in p-Si under a fixed reverse bias of −1.0 V (**e**), in n-Si under a fixed bias of −1.0 V (**g**), in TiO_2 under a fixed bias of −1.0 V (**i**), in NSTO under a fixed bias of −2.0 V (**k**) and increased contact loading forces, respectively. Scale bars, 50 nm. **d**,**f**,**h**,**j**,**l**, The corresponding absolute average current variations versus loading force calculated from the statistical distributions of the values of the current mappings shown in **c**,**e**,**g**,**i**,**k**, which displays the stress and/or strain modulation process on electrical transport. The results of mechanical 2D scanning are consistent with the results of static measurement, further demonstrating the flexoelectronic effect in centrosymmetric semiconductors. The different colours in **d**,**f**,**h**,**j**,**l**, show the corresponding average current variations of different semiconductors during the mechanical 2D scanning processes. Error bars indicate standard deviations.

of the flexoelectronic effect in bulk centrosymmetric semiconductors, including covalent crystals and ionic crystals, under static nanoindentation.

To gain an insight into the dynamics of the flexoelectronic effect, we performed conventional two-dimensional scanning via conductive AFM with tip motion along the surface of various semiconductors, including Si, TiO_2 and NSTO (Fig. 5a,b). A trailing flexoelectric polarization field can be effectively induced by the strain gradient beneath the tip via flexoelectricity, and is much larger with tip motion than that in the static case[29]. When the trailing flexoelectric field is large enough to affect the local metal–semiconductor contacts by exerting a substantial influence on the modulation of electronic charges in the interface states, switching electronics is enabled by controlling the tip scanning force. Figure 5c,e,g,i,k shows current mapping images of Si, TiO_2 and NSTO during mechanical scanning at fixed bias and various scanning forces with accurately determined values over the $0.2 \times 0.2\ \mu m^2$ areas (Supplementary Figs. 15–19). The corresponding absolute average current variations versus scanning forces are calculated from the statistical distributions of the values of current mappings, which display the mechanical modulation

process of the electrical transport across the metal–semiconductor contacts (Fig. 5d,f,h,j,l). Similar to the static electrical characteristic measurements, the current in p-Si increases gradually under both positive and negative bias, whereas the current first increases and then decreases in n-Si, TiO_2 and NSTO with increased scanning forces. Although not every pixel is modulated effectively, possibly owing to localized changes in contact caused by the surface unevenness of the samples during dynamic scanning, the flexoelectronic effect in these centrosymmetric semiconductors is nevertheless obvious and can be further improved in the future through design adjustment. Furthermore, dynamic flexoelectronics by mechanical two-dimensional scanning offers a response time <4 ms and a pixel size of 0.78 nm, which is promising for the design of future electronic devices with fast responses and high resolutions. This statistical approach eliminates the issues caused by artificiality and satisfactorily demonstrates that a dynamic flexoelectric polarization field can be used as an effective but simple route for the mechanically tunable electronics. Other factors, such as surface charges and the triboelectric effect during the mechanical scanning process, may have some influence on the results but do not play a major role (Supplementary Notes 6 and 7, and Supplementary Figs. 20–23).

The flexoelectronic effect differs from, but is closely related to, the piezotronic effect[19–22] (Supplementary Figs. 24 and 25). These two effects are both interface effects that use polarization charges to asymmetrically modulate local Schottky contacts at different metal–semiconductor terminals. The piezotronic effect manifests only in piezoelectric/ferroelectric semiconductors regardless of whether there is a strain gradient, whereas the strain-gradient-induced flexoelectronic effect can be realized in any semiconductor regardless of its crystal structure. In addition, the magnitude of tuning by the piezotronic effect can be much more effective than the flexoelectronic effect in centrosymmetric crystals. In piezoelectric semiconductors, the piezoelectric polarization charges are only present within one or two atomic layers of the surface, and therefore mainly affect the electronic charges at the metal–semiconductor interface, while flexoelectric polarization, which depends on the magnitude of the strain gradient, is distributed inside the semiconductor over a range of lengths or volumes and will exert a substantial influence on the concentration and distribution of free carriers of semiconductors near the interface. The flexoelectronic effect therefore seems to be an integration of the piezotronic effect over a length or volume or area, that is, an 'integration' of many piezotronic segments, which is similar to integration and differentiation in calculus. At the same time, it should be pointed out that those materials exhibiting a piezotronic effect also exhibit a flexoelectronic effect.

We have demonstrated a strong flexoelectronic effect in centrosymmetric semiconductors, in which the band structure and hence the electrical transport can be effectively modulated by flexoelectric polarization. Active electronics based on centrosymmetric semiconductors with high strain sensitivity, fast response and high resolution have been achieved. The effectiveness and universality of the flexoelectronic effect show promise for semiconductor-based electronic device design and electromechanical applications. This study also has the potential to stimulate new research on semiconductor-based flexoelectric technology, such as enhanced solar technology[30], stretchable electronics/optoelectronics, and hybrid spintronics and valleytronics (Supplementary Fig. 26 and Supplementary Note 8).

Online content

Any methods, additional references, Nature Research reporting summaries, source data, extended data, supplementary information, acknowledgements, peer review information; details of author contributions and competing interests; and statements of data and code availability are available at https://doi.org/10.1038/s41565-020-0700-y.

Received: 5 January 2020; Accepted: 27 April 2020;
Published online: 22 June 2020

References

1. Wu, W. Z., Wen, X. N. & Wang, Z. L. Taxel-addressable matrix of vertical-nanowire piezotronic transistors for active and adaptive tactile imaging. *Science* **340**, 952–957 (2013).
2. Wu, W. Z. et al. Piezoelectricity of single-atomic-layer MoS_2 for energy conversion and piezotronics. *Nature* **514**, 470–474 (2014).
3. Pan, C. F. et al. High-resolution electroluminescent imaging of pressure distribution using a piezoelectric nanowire LED array. *Nat. Photon.* **7**, 752–758 (2013).
4. Qi, J. J. et al. Piezoelectric effect in chemical vapour deposition-grown atomic-monolayer triangular molybdenum disulfide piezotronics. *Nat. Commun.* **6**, 7430 (2015).
5. Stewart, J. W., Vella, J. H., Li, W., Fan, S. & Mikkelsen, M. H. Ultrafast pyroelectric photodetection with on-chip spectral filters. *Nat. Mater.* **19**, 158–162 (2019).
6. Wang, Z., Yu, R., Pan, C., Li, Z., Yang, J., Yi, F. & Wang, Z. L. Light-induced pyroelectric effect as an effective approach for ultrafast ultraviolet nanosensing. *Nat. Commun.* **6**, 8401 (2015).
7. Maksymovych, P., Jesse, S., Yu, P., Ramesh, R., Baddorf, A. P. & Kalinin, S. V. Polarization control of electron tunneling into ferroelectric surfaces. *Science* **324**, 1421–1425 (2009).
8. Garcia, V. et al. Ferroelectric control of spin polarization. *Science* **327**, 1106–1110 (2010).
9. Zhang, Y. et al. Anisotropic polarization-induced conductance at a ferroelectric–insulator interface. *Nat. Nanotechnol.* **13**, 1132–1136 (2018).
10. Kogan, S. M. Piezoelectric effect during inhomogeneous deformation and acoustic scattering of carriers in crystals. *Sov. Phys. Solid State* **5**, 2069–2070 (1964).
11. Bursian, E. & Zaikovskii, O. I. Changes in curvature of ferroelectric film due to polarization. *Sov. Phys. Solid State* **10**, 1121 (1968).
12. Catalan, G. et al. Flexoelectric rotation of polarization in ferroelectric thin films. *Nat. Mater.* **10**, 963–967 (2011).
13. Lu, H. et al. Mechanical writing of ferroelectric polarization. *Science* **336**, 59–61 (2012).
14. Trung, T. Q. & Lee, N. E. Flexible and stretchable physical sensor integrated platforms for wearable human-activity monitoring and personal healthcare. *Adv. Mater.* **28**, 4338–4372 (2016).
15. Bhaskar, U. K., Banerjee, N., Abdollahi, A., Wang, Z., Schlom, D. G., Rijnders, G. & Catalan, G. A flexoelectric microelectromechanical system on silicon. *Nat. Nanotechnol.* **11**, 263–266 (2016).
16. Wen, X., Li, D., Tan, K., Deng, Q. & Shen, S. P. Flexoelectret: an electret with a tunable flexoelectriclike response. *Phys. Rev. Lett.* **122**, 148001 (2019).
17. Das, S. et al. Enhanced flexoelectricity at reduced dimensions revealed by mechanically tunable quantum tunneling. *Nat. Commun.* **10**, 537 (2019).
18. Narvaez, J., Vasquez-Sancho, F. & Catalan, G. Enhanced flexoelectric-like response in oxide semiconductors. *Nature* **538**, 219–221 (2016).
19. Wang, Z. L. Nanopiezotronics. *Adv. Mater.* **19**, 889–892 (2007).
20. Wu, W. Z. & Wang, Z. L. Piezotronics and piezo-phototronics for adaptive electronics and optoelectronics. *Nat. Rev. Mater.* **1**, 16031 (2016).
21. Zhang, Y., Liu, Y. & Wang, Z. L. Fundamental theory of piezotronics. *Adv. Mater.* **23**, 3004–3013 (2011).
22. Wang, Z. L. & Wu, W. Z. Piezotronics and piezo-phototronics: fundamentals and applications. *Natl Sci. Rev.* **1**, 62–90 (2014).
23. Fischer-Cripps, A. C *Introduction to Contact Mechanics* (Springer, 2000).
24. Zubko, P., Catalan, G., Buckley, A., Welche, P. R. L. & Scott, J. F. Strain-gradient-induced polarization in $SrTiO_3$ single crystal. *Phys. Rev. Lett.* **99**, 167601 (2007).
25. Hong, J. W. & Vanderbilt, D. First-principles theory and calculation of flexoelectricity. *Phys. Rev. B* **88**, 174107 (2013).
26. Amjadi, M., Kyung, K. U., Park, I. & Sitti, M. Stretchable, skin-mountable, and wearable strain sensors and their potential applications: a review. *Adv. Funct. Mater.* **26**, 1678–1698 (2016).
27. Conley, H. J. et al. Bandgap engineering of strained monolayer and bilayer MoS_2. *Nano Lett.* **13**, 3626–3630 (2013).
28. Gao, Y. & Wang, Z. L. Equilibrium potential of free charge carriers in a bent piezoelectric semiconductive nanowire. *Nano Lett.* **9**, 1103–1110 (2009).
29. Park, S. M. et al. Selective control of multiple ferroelectric switching pathways using a trailing flexoelectric field. *Nat. Nanotechnol.* **13**, 366–370 (2018).
30. Chu, K. et al. Enhancement of the anisotropic photocurrent in ferroelectric oxides by strain gradients. *Nat. Nanotechnol.* **10**, 972–979 (2015).

Methods

Materials. The p-type Si wafers (B-doped (100) wafers, ~10 Ω cm and ~0.001–0.005 Ω cm) and n-type Si wafers (As-doped (100) wafers, ~10 Ω cm and ~0.0010.005 Ω cm) were from University Wafer. The (100)-oriented rutile TiO_2 single crystals were from Sigma-Aldrich. The 0.05% Nb-doped $SrTiO_3$ (100) NSTO single crystals were from MTI. The dimensions of TiO_2 and NSTO were 10 mm × 10 mm × 0.5 mm (length × width × thickness). All of the crystals were washed in an ultrasonicator with acetone, isopropyl alcohol and distilled water for 15 min each, and then vacuum dried. The Si wafers were etched in buffered HF solution for 5 min before measurements were obtained.

Single-point electrical transport measurements under tip force. The electrical transport characterizations of cubic-structured Si and centrosymmetric semiconductors (TiO_2, NSTO) under a tip force were measured with an Asylum Research MFP-3D atomic force microscope with ORCA mode (conductive AFM). Conductive Pt/Ir-coated atomic force microscope tips with a radius of ~25 nm and spring constants of ~30–50 N m^{-1}, and the ORCA module with measurement ranges of 2 nA, 20 nA and 20 μA, were used to apply compressive forces and simultaneously measure the current. An electrical bias was applied through the substrate, which was swiped at a ramping rate of ~1.0 V s^{-1}. The background noise is lower than ±10 pA and ±50 pA in the 2 nA and 20 nA measurement ranges, respectively. To characterize the electrical transport characteristics of the flexoelectronic devices under different tip forces, each experiment involved three steps. (1) The AFM tip was placed in contact with the surface of the crystal with a preset force. The applied force was increased by further deflecting the AFM tip cantilever. (2) After the applied force reached a preset value, the compressive force was maintained constant by the feedback amplifier circuit of the ARC2 controller, and then the electrical measurements were initiated. In this stage, a sweeping bias was applied between the substrate and the tip. (3) After the I–V measurement had been performed, a new compressive force was applied by setting a new target setpoint value and the corresponding electrical measurement was performed. The AFM tips are calibrated by the thermal noise method. We can precisely obtain the inverse optical lever sensitivity (InvOLS) and the spring constant of the tips. The precise force is calculated by multiplying the spring constant, InvOLS and cantilever deflection (force = spring constant × InvOLS × (preset deflection − initial deflection)). All measurements were performed in air at room temperature. The gauge factor is defined as: $GF = (\Delta I/I)/\Delta\varepsilon$, $\sigma = E\varepsilon$, where I, ε, σ and E represent the current, the strain, the normal pressure, and the effective Young's modulus, respectively.

Two-dimensional scanning electrical transport measurements. The dynamic flexoelectronics in centrosymmetric semiconductor by mechanical 2D scanning were performed using conductive AFM under fixed bias and various scanning forces with accurately determined values over areas. The scanning zones corresponding to all current mapping images in each scanning series are the same area. By setting a preset force, a scan range and a scan rate, the mechanical 2D mappings of preset compressive forces were applied to the experimental crystals (Si, TiO_2 and NSTO). Meanwhile, a constant electrical bias was applied through the crystals to provide the power. At the same time, the current amplifier in the ORCA module was utilized to measure the corresponding current flow through the Schottky contact formed between the conductive tip and the crystals. During the mechanical scanning process, the preset force remained constant by controlling the bending degree of the microscope tip cantilever. All measurements were performed in air at room temperature.

Theoretical simulations of the strain distributions in centrosymmetric semiconductors. The Hertz contact mechanics of a spherical indenter are used here to investigate the strain distribution and strain-gradient-induced flexoelectric polarization distribution of centrosymmetric semiconductors under a mechanically loaded tip-force model[23]. The spatial distributions of strain and strain-gradient were calculated by the theory of potential introduced by Boussinesq and Cerruti. Here the normal pressure distribution beneath a spherical indenter given by Hertz was used:

$$\frac{\sigma_z(r)}{p_m} = -\frac{3}{2}\left(1-\frac{r^2}{a^2}\right)^{\frac{1}{2}} \quad r \le a \tag{1}$$

where p_m is the mean pressure on the contact surface, σ_z is the normal pressure and a is the contact radius, respectively. The radius and depth of contact area under load F are given by:

$$a = \sqrt{Rh} \tag{2}$$

$$h = \left(\frac{3F}{4E\sqrt{R}}\right)^{2/3} \tag{3}$$

where R is the radius of the indenter and E is the effective Young's modulus. With a point force F_0 on the origin, the stress components can be given by:

$$\sigma_x = \frac{F_0}{2\pi}\left[\frac{1-2\nu}{r^2}\left(\left(1-\frac{z}{\rho}\right)\frac{x^2-y^2}{r^2}+\frac{zy^2}{\rho^3}\right)-\frac{3zx^2}{\rho^5}\right] \tag{4}$$

$$\sigma_y = \frac{F_0}{2\pi}\left[\frac{1-2\nu}{r^2}\left(\left(1-\frac{z}{\rho}\right)\frac{y^2-x^2}{r^2}+\frac{zx^2}{\rho^3}\right)-\frac{3zy^2}{\rho^5}\right] \tag{5}$$

$$\sigma_z = -\frac{3F_0}{2\pi}\frac{z^3}{\rho^5} \tag{6}$$

$$\tau_{xy} = \frac{F_0}{2\pi}\left[\frac{1-2\nu}{r^2}\left(\left(1-\frac{z}{\rho}\right)\frac{xy}{r^2}-\frac{xyz}{\rho^3}\right)-\frac{3xyz}{\rho^5}\right] \tag{7}$$

$$\tau_{xz} = -\frac{3F_0}{2\pi}\frac{xz^2}{\rho^5} \tag{8}$$

$$\tau_{yz} = -\frac{3F_0}{2\pi}\frac{yz^2}{\rho^5} \tag{9}$$

where ν is the Poisson's ratio, $r^2 = x^2 + y^2$, and $\rho = (x^2 + y^2 + z^2)^{1/2}$.

According to the principle of superposition, the strain distribution under a spherical indenter can be given in cylindrical coordinates by:

$$\frac{\sigma_r}{p_m} = \frac{3}{2}\left\{\frac{1-2\nu}{3}\frac{x^2}{r^2}\left[1-\left(\frac{z}{u^{1/2}}\right)^3\right]+\left(\frac{z}{u^{1/2}}\right)^3\frac{a^2u}{u^2+a^2z^2} + \frac{z}{u^{1/2}}\left[\frac{u(1-\nu)}{a^2+u}+(1+\nu)\frac{u^{1/2}}{a}\tan^{-1}\left(\frac{z}{u^{1/2}}\right)-2\right]\right\} \tag{10}$$

$$\frac{\sigma_\theta}{p_m} = -\frac{3}{2}\left\{\frac{1-2\nu}{3}\frac{x^2}{r^2}\left[1-\left(\frac{z}{u^{1/2}}\right)^3\right] + \frac{z}{u^{1/2}}\left[2\nu+\frac{u(1-\nu)}{a^2+u}-(1+\nu)\frac{u^{1/2}}{a}\tan^{-1}\left(\frac{z}{u^{1/2}}\right)\right]\right\} \tag{11}$$

$$\frac{\sigma_z}{p_m} = -\frac{3}{2}\left(\frac{z}{u^{1/2}}\right)^3\left(\frac{a^2u}{u^2+a^2z^2}\right) \tag{12}$$

$$\frac{\tau_{rz}}{p_m} = -\frac{3}{2}\left(\frac{rz^2}{u^2+a^2z^2}\right)\left(\frac{a^2u^{1/2}}{u+a^2}\right) \tag{13}$$

$$u = \frac{1}{2}\left\{\left(r^2+z^2-a^2\right)+\left[\left(x^2+y^2+z^2\right)^2+4a^2z^2\right]^{1/2}\right\} \tag{14}$$

where σ_r is the radial stress distribution. With Hooke's law, the strain distribution can be obtained by[31]

$$\varepsilon_i = \frac{1}{E}\left[\sigma_i - \nu(\sigma_j+\sigma_k)\right] \tag{15}$$

$$\varepsilon_{ij} = \frac{1+\nu}{E}\tau_{ij} \tag{16}$$

where i, j and k represent the x, y and z axes with different values, respectively. In our calculation, we set the Poisson's ratio to 0.2, 0.24 and 0.27 for Si, rutile-TiO_2 and $SrTiO_3$, respectively, and the effective Young's modulus to 188 GPa, 210 GPa and 264 GPa for Si, rutile-TiO_2 and $SrTiO_3$, respectively. The mechanically loaded tip force is 25 μN and the tip radius is 25 nm.

The calculated strain distribution in the centrosymmetric semiconductors Si, TiO_2 and $SrTiO_3$ in both the x and z components, and its derivative with respect to z under a force of ~25 μN with a tip radius of 25 nm, at the origin are shown in Fig. 1b and Supplementary Figs. 1 and 2, respectively. However, it should be noted that the spherical indenter is assumed to be rigid in the theoretical model, whereas in the actual experiment the atomic force microscope tips are not ideally rigid. Hence, the strain gradient in the experiment is smaller than the theoretical results. We can, however, still induce an effective strain on the semiconductor surface by applying the microscope tip, since a tip with a large force constant is highly rigid.

Theoretical simulations of the polarization distribution in centrosymmetric semiconductors. Considering the coupling between the electric polarization and the strain gradient, direct flexoelectric polarization distributions of semiconductors under a mechanically loaded tip-force can be described as[32]:

$$P_i = u_{ijkl}\frac{\partial\varepsilon_{jk}}{\partial x_l} \tag{17}$$

where P_i is the polarization, u_{ijkl} is the flexoelectric coefficient and $x_l = x, y, z$. With the obtained polarization, one can then calculate the flexoelectric charge density through[33]:

$$q = -\nabla \cdot P \tag{18}$$

Here, earlier symmetry-adapted flexoelectric coefficients are applied. For Si and $SrTO_3$, the non-zero flexoelectric coefficients include three independent coefficients, $\mu_{1111}=\mu_{2222}=\mu_{3333}$, $\mu_{1122}=\mu_{1133}=\mu_{2211}=\mu_{2233}=\mu_{3311}=\mu_{3322}$ and $\mu_{1221}=\mu_{1331}=\mu_{2112}=\mu_{2332}=\mu_{3113}=\mu_{3223}$. For rutile-$TiO_2$, the corresponding eight independent coefficients are $\mu_{1111}=\mu_{2222}$, $\mu_{1122}=\mu_{2211}$, $\mu_{1221}=\mu_{2112}$, $\mu_{1133}=\mu_{2233}$, $\mu_{1331}=\mu_{2332}$, $\mu_{3113}=\mu_{3223}$, $\mu_{3311}=\mu_{3322}$ and μ_{3333}, respectively. Supplementary Table 2 shows the assumed corresponding flexoelectric coefficients of the semiconductors in our calculation.

It should be noted that the flexoelectric coefficients μ_{ijkl} are not known with certainty due to the difficulty of extracting these coefficients from the experiment, and orders-of-magnitude discrepancies may exist between experiment and theory for a variety of reasons[18,25,34]. We also note that a hidden symmetry was proposed in the flexoelectric tensor, which allows a further reduction of the independent coefficients[35].

Theoretical simulation of the modulation effect of flexoelectric polarization on the electrical transport property. To fully demonstrate the flexoelectronic effect in centrosymmetric semiconductors, we investigate the modulatory effect of flexoelectric polarization charges on the Schottky contact and calculate the current density across the Schottky contact via COMSOL Multiphysics version 3.5.

The drift-diffusion model is applied through the electrostatic and convection-diffusion modules. The following assumptions are adopted in our calculation: (1) the barrier height is much larger than k_BT, where k_B is the Boltzmann constant and T is the temperature; (2) electron collisions only occur in the depletion region; (3) the carrier concentrations at the boundaries are not affected by the current; (4) the impurity concentrations are non-degenerate. Basic equations for drift-diffusion model include:

$$\begin{cases} -\nabla \cdot (\varepsilon_s \nabla \psi_i) = q(p - n + N) \\ -\nabla \cdot J_n = -qR_{\mathrm{SRH}} \\ -\nabla \cdot J_p = qR_{\mathrm{SRH}} \end{cases} \tag{19}$$

where ε_s is the dielectric constant, ψ_i is the electrostatic potential, p and n denote the hole and electron concentrations, respectively, N stands for the fixed charge associated with doping and J_n and J_p represent the electron and hole current density, respectively. R_{SRH} is the Shockley–Read–Hall recombination, which reads:

$$R_{\mathrm{SRH}} = \frac{np - n_i^2}{\tau_p(n + n_1) + \tau_n(p + p_1)} \tag{20}$$

where $\tau_{n(p)}$ is the carrier lifetime, n_i is the intrinsic carrier concentration, n_1 and p_1 are the trap-level-related electron and hole concentrations, respectively. The current densities are given by:

$$\begin{cases} J_n = q\mu_n nE + qD_n \nabla n \\ J_p = q\mu_p pE - qD_p \nabla p \end{cases} \tag{21}$$

where $\mu_{n(p)}$ is the electron (hole) mobility and $D_{n(p)}$ is the electron (hole) diffusion coefficient.

One more term is considered in the Poisson's equation for the flexoelectronic effect, which results in:

$$-\nabla \cdot (\varepsilon_s \nabla \psi_i) = q(p - n + N + \rho_f) \tag{22}$$

where ρ_f represents the flexoelectric polarization charges near the tip–surface contact. For the negative polarization charges in our simulations, the distribution on the centre line is taken to be within a depth x_d, which denotes the boundary of negative charge. Nonlinear function fitting is applied to formulate the distribution, which results in:

$$\rho_f = \rho_m \left[1 + \frac{x}{x_0}\right]^{-1} \quad x \le x_d \tag{23}$$

where ρ_m denotes the peak charge density near the contact and x_0 characterizes the decay of charge distribution. It is also appropriate to assume that the decay of charge distribution varies within the materials.

Supplementary Tables 3 and 4 show the corresponding parameters of the semiconductors in the theoretical model for the qualitative simulations. Three points should be noted here. (1) To facilitate the simulations, we have simplified and idealized some set conditions in the theoretical calculation. In fact, the tip–surface contact area will increase under increased loading forces. To simplify the theoretical model, we have not considered it in the calculation. (2) The flexoelectric polarization charges will not only present on the material surface but are also distributed inside the crystal over a range of lengths and volumes. However, to make the calculation results converge, we assume that the flexoelectric polarization charges are distributed near the contact interface. (3) The parameters of these semiconductors for COMSOL Multiphysics simulations may not be completely consistent with those of the materials used in the experiments, but the theoretical results nevertheless reflect the modulatory effect of flexoelectric polarization charges on electron concentration, the energy band and hence electrical transport.

Data availability

The data that support the plots within this paper and other findings of this study are available from the corresponding author upon reasonable request.

References

31. Landau, L. D., Pitaevskii L. P., Kosevich, A. M., Lifshitz, E.M. *Theory of Elasticity* (Elsevier, 1986).
32. Yudin, P. V. & Tagantsev, A. K. Fundamentals of flexoelectricity in solids. *Nanotechnology* **24**, 432001 (2013).
33. Očenášek, J. et al. Nanomechanics of flexoelectric switching. *Phys. Rev. B* **92**, 035417 (2015).
34. Zubko, P., Catalan, G. & Tagantsev, K. T. Flexoelectric effect in solids. *Annu. Rev. Mater. Res.* **43**, 387–421 (2013).
35. Eliseev, E. A. & Morozovska, A. N. Hidden symmetry of flexoelectric coupling. *Phys. Rev. B* **98**, 094108 (2018).

Acknowledgements

We thank Q. Xu and S. Xu for helpful discussion. This research was supported by the National Key R&D Project from Minister of Science and Technology (grant number 2016YFA0202704), Beijing Municipal Science and Technology Commission (grant numbers Z171100000317001, Z171100002017017, Y3993113DF) and the National Natural Science Foundation of China (grant numbers 11704032, 51432005, 5151101243, 51561145021, 51322203 and 51472111).

Author contributions

Z.L.W., L.W., Y.Q. and S.L conceived the project. Z.L.W., L.W., Y.Q. and S.L. designed the experiments. L.W. and S.L. performed the experiments and analysed the results. X.F and C.Z performed the theoretical calculations and analysis. L.Z and J.Z provided assistance with the experiments. All authors contributed to discussions and to writing the manuscript.

Competing interests

The authors declare no competing interests.

Additional information

Supplementary information is available for this paper at https://doi.org/10.1038/s41565-020-0700-y.

Correspondence and requests for materials should be addressed to Y.Q. or Z.L.W.

Peer review information *Nature Nanotechnology* thanks Shanming Ke and Sang-Woo Kim for their contribution to the peer review of this work.

Reprints and permissions information is available at www.nature.com/reprints.